World Electric Vehicle Journal

Article

Direct Power Control of a Bipolar Output Active Rectifier for More Electric Aircraft Based on an Optimized Sector Division

Yajun Zhao *, Wenxin Huang and Feifei Bu

College of Automation Engineering, Nanjing University of Aeronautics and Astronautics, Nanjing 210016, China
* Correspondence: zhaoyajun@nuaa.edu.cn

Abstract: This paper presents a novel direct power control (DPC) strategy based on an optimized sector division for a three-phase coupled inductor-based bipolar output active rectifier (TCIBAR) applied in more electric aircraft (MEA). First, based on the instantaneous power theory, the power model of the TCIBAR is built in the synchronous rotating coordinate system. Second, to implement the hysteresis power control of TCIBAR without causing the runaway of the zero-sequence current in the three-phase coupled inductor (TCI), a set of new voltage vectors that have the same zero-sequence voltage (ZSV) component are synthesized and adopted in the proposed DPC strategy. Third, by quantitatively analyzing the effect of the new synthesized voltage vectors on the power variation of TCIBAR, an optimized sector division method is proposed to improve the accuracy of power control and reduce the phase current harmonics in TCIBAR. Finally, to maintain the voltage balance of the bipolar dc ports in TCIBAR, voltage balance control is studied in the proposed DPC strategy. The proposed DPC strategy is researched on an experimental platform of TCIBAR, and the results show that the proposed DPC strategy is feasible and has good static and dynamic performance.

Keywords: direct power control; sector division; bipolar-output active rectifier; more electric aircraft

check for updates

Citation: Zhao, Y.; Huang, W.; Bu, F. Direct Power Control of a Bipolar Output Active Rectifier for More Electric Aircraft Based on an Optimized Sector Division. *World Electr. Veh. J.* **2023**, *14*, 89. https://doi.org/10.3390/wevj14040089

Academic Editors: Jianfei Chen, Liyan Zhu, Chen Duan and Haibo Huang

Received: 9 March 2023
Revised: 25 March 2023
Accepted: 27 March 2023
Published: 30 March 2023

Copyright: © 2023 by the authors. Licensee MDPI, Basel, Switzerland. This article is an open access article distributed under the terms and conditions of the Creative Commons Attribution (CC BY) license (https://creativecommons.org/licenses/by/4.0/).

1. Introduction

With the aggravation of environmental pollution and the depletion of fossil energy, the development of aircraft electrification has attracted increasing attention from researches in recent decades [1–3], and more electric aircraft (MEA) is considered a promising scheme to improve the energy efficiency and reduce the fuel consumption of aircrafts [4,5]. In MEAs, the pneumatic, hydraulic, and mechanical energies are replaced by electrical energy, either partially or completely, and an increase in electrical energy use can create advantages, such as higher efficiency, lower weight, and higher reliability of the aircraft [6–8]. Since the proportion of electrical energy in aircraft secondary energy has greatly increased, the electrical power system (EPS) plays a vital role in MEA [9]. In recent years, much research has been done on the architecture of the EPS for MEA [10–13], and the ±270 V high-voltage direct current (HVDC) power system is promising architecture for future MEAs [14–16].

In current MEAs, such as the Boeing 787, an auto transformer rectifier unit (ATRU) is usually used to rectify the AC power of the generator and provide ±270 V bipolar DC power [12,14]. The ATRU consists of an autotransformer and diode bridge rectifiers and is a passive rectifier which has a simple structure and high reliability [17–19]. However, the ATRU greatly increases the weight and volume of the EPS and cannot actively regulate the output voltages. In addition, the ATRU cannot guarantee the voltage balance between its bipolar DC outputs under unbalanced load conditions. Therefore, the ATRU cannot meet the demands of growing electrical loads in future MEAs, and the bipolar output active rectifier is a competitive alternative to establish the bipolar DC power system for MEAs [20]. In recent years, a three-phase coupled inductor-based bipolar output active rectifier (TCIBAR) has been proposed and researched to generate symmetrical bipolar DC power supply [20–22]. The topology of the TCIBAR is composed of a two-level voltage source converter (VSC) and a three-phase coupled inductor (TCI) which is connected between the neutral points of the three-phase bridges and DC-side split capacitors [21]. Meanwhile, the TCI is used to provide a current injection path to the neutral point of the split capacitors and realize the voltage balance control of the bipolar DC ports. As a novel topology, the TCIBAR has advantages of simple topology, flexible control, and high reliability [20], but presently, there are few studies on the control strategy of TCIBAR. A basic control structure is built for TCIBAR in [21], but it does not delve into the control principle and operation performance of TCIBAR. In [20], the effect mechanism of the zero-sequence voltage (ZSV) in the DC voltage balance control of TCIBAR is analyzed, and a DC voltage balancing strategy based on zero vector redistribution is proposed for TCIBAR. These two control strategies are based on the architecture of voltage–oriented control (VOC). The VOC strategy has excellent steady-state performance, but its dynamic response is limited by the performance of the inner current loop [23,24].

Direct power control (DPC) is another high-performance control strategy along with VOC. In DPC, active and reactive power can be directly controlled by selecting the appropriate voltage vectors from a pre-defined switching table [25,26]. Compared with VOC, DPC requires neither the inner current loop nor the voltage modulation module [27,28] and can be realized based on bang-bang control, which brings the advantages of easy implementation and excellent dynamic performance [29–32]. The application of DPC in TCIBAR can retain the advantages of both and be a good scheme to provide balanced bipolar DC power supply for MEA. However, the zero-sequence components, which play an important role in the control of TCIBAR [20], are not taken into account in the classic DPC. Meanwhile, the classic DPC does not involve the voltage balance control between the bipolar DC ports. In addition, the DPC strategies in most literatures adopt the conventional 12-sector division method proposed in [25] to establish the switching table, but the basic mechanism is not analyzed, and the effect of voltage vectors on power variation is only analyzed qualitatively based on space vector diagram, which may lead to a false control command at some intervals [23]. Therefore, the classic DPC cannot be applied to the TCIBAR directly, and the traditional 12-sector division method may not be the best choice for the DPC of TCIBAR.

In this paper, a DPC strategy based on optimized sector division is proposed for TCIBAR, and the innovations of the proposed DPC strategy are summarized as follows.

1. A set of new voltage vectors are synthesized in the proposed DPC strategy to extend the eight basic voltage vectors. Based on the new synthesized voltage vectors, the zero-sequence current in TCI can be controlled in a stable manner while implementing the hysteresis power control of the TCIBAR.
2. Based on the derived power model of TCIBAR in the synchronous rotating coordinate system, the effect of the new synthesized voltage vectors on the power variation of TCIBAR is quantitatively analyzed. On this basis, an optimized sector division method is proposed to establish a new switching table for TCIBAR, which can improve the quality of the phase currents in TCIBAR.
3. A ZSV generation method is developed in the proposed DPC strategy. Based on the ZSV generation method, the voltage balance control of the bipolar DC ports in TCIBAR can be realized, even under unbalanced load conditions.

The rest of this paper is arranged as follows. The power model of the TCIBAR in the synchronous rotating coordinate system is derived in Section 2, and Section 3 presents the introduction of the proposed DPC strategy. Steady-state and dynamic experimental research on the proposed DPC strategy are shown in Section 4. Finally, conclusions are drawn in Section 5.

2. TCIBAR Model Based on Instantaneous Power Theory

To realize the effective control of the TCIBAR, it is necessary to establish the mathematical model of the TCIBAR first. The topology of TCIBAR is shown in Figure 1, where R_s and R are the winding resistance of the source inductor and the TCI; e_a, e_b, and e_c are the three-phase AC source voltages; i_{sa}, i_{sb}, and i_{sc} are the three-phase input currents; i_{la}, i_{lb}, and i_{lc} are the three-phase currents in TCI; u_p and u_n are the port voltages; i_p and i_n are the load currents of positive and negative ports; and U_{dc} is the total DC bus voltage.

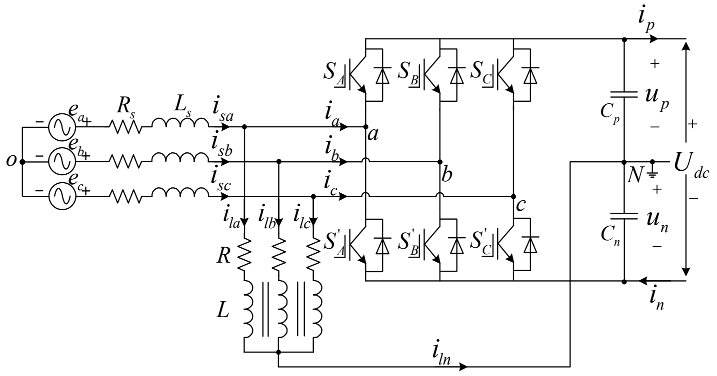

Figure 1. Topology diagram of the TCIBAR.

According to Figure 1, the voltage equations for the source inductor in the $dq0$ synchronous rotating coordinate system can be expressed as Equation (1),

$$\begin{bmatrix} e_d \\ e_q \\ e_0 \end{bmatrix} = L_s \frac{d}{dt} \begin{bmatrix} i_{sd} \\ i_{sq} \\ i_{s0} \end{bmatrix} + \begin{bmatrix} 0 & -\omega L_s & 0 \\ \omega L_s & 0 & 0 \\ 0 & 0 & 0 \end{bmatrix} \begin{bmatrix} i_{sd} \\ i_{sq} \\ i_{s0} \end{bmatrix} + R_s \begin{bmatrix} i_{sd} \\ i_{sq} \\ i_{s0} \end{bmatrix} + \begin{bmatrix} u_d \\ u_q \\ u_0 \end{bmatrix} \tag{1}$$

where e_d, e_q, e_0, i_{sd}, i_{sq}, i_{s0}, and u_d, u_q, u_0 are the d-axis, q-axis, and zero-sequence components of source voltages, input currents, and VSC voltages, respectively, and ω is the angular frequency of the AC source. The zero-sequence equation in Equation (1) can be ignored since $i_{s0} = 0$.

Based on the instantaneous power theory, the instantaneous power of the TCIBAR can be calculated in the dq coordinate system as follows:

$$\begin{cases} p = e_d i_{sd} + e_q i_{sq} \\ q = e_q i_{sd} - e_d i_{sq} \end{cases} \tag{2}$$

where p and q are the instantaneous active and reactive power of TCIBAR, respectively.

By taking the derivative of Equation (2), the power variation rate of the TCIBAR can be obtained as follows:

$$\begin{cases} \frac{dp}{dt} = i_{sd}\frac{de_d}{dt} + e_d\frac{di_{sd}}{dt} + i_{sq}\frac{de_q}{dt} + e_q\frac{di_{sq}}{dt} \\ \frac{dq}{dt} = i_{sd}\frac{de_q}{dt} + e_q\frac{di_{sd}}{dt} - i_{sq}\frac{de_d}{dt} - e_d\frac{di_{sq}}{dt} \end{cases} \tag{3}$$

By substituting Equations (1) and (2) into Equation (3) and regarding the AC source as an ideal voltage source, the power model of the TCIBAR can be deduced as:

$$\begin{cases} L_s\frac{dp}{dt} = -R_s p - \omega L_s q - (e_d u_d + e_q u_q) + e_d^2 + e_q^2 \\ L_s\frac{dq}{dt} = -R_s q + \omega L_s p - (e_q u_d - e_d u_q) \end{cases} \tag{4}$$

Then, by orienting the d-axis of the synchronous coordinate system to the AC source voltage vector, the q-axis component of the AC source voltage (e_q) is equal to zero. Meanwhile, by ignoring some small components in Equation (4), the simplified power model of the TCIBAR can be obtained, as expressed in Equation (5).

$$\begin{cases} L_s\frac{dp}{dt} = -e_d u_d + e_d^2 \\ L_s\frac{dq}{dt} = e_d u_q \end{cases} \tag{5}$$

Next, since the zero-sequence current in the TCI can be regulated to realize the voltage balance control of the bipolar DC ports [20], the zero-sequence component of the TCI should be considered in the modeling of the TCIBAR. In the TCI, a balanced three-phase magnetic core can be used to reduce the chance of core saturation since it cannot carry the zero-sequence DC flux [21]. On this basis, the voltage equations for the TCI can be deduced, as shown in Equation (6),

$$\begin{bmatrix} L & -M & -M \\ -M & L & -M \\ -M & -M & L \end{bmatrix} \frac{d}{dt} \begin{bmatrix} i_{la} \\ i_{lb} \\ i_{lc} \end{bmatrix} + \begin{bmatrix} R & 0 & 0 \\ 0 & R & 0 \\ 0 & 0 & R \end{bmatrix} \begin{bmatrix} i_{la} \\ i_{lb} \\ i_{lc} \end{bmatrix} = \begin{bmatrix} u_{aN} \\ u_{bN} \\ u_{cN} \end{bmatrix} \tag{6}$$

where L and M are the self-inductance and mutual inductance of the TCI, respectively, and u_{aN}, u_{bN}, and u_{cN} are the three-phase voltages of the TCI.

By applying the Park transformation to Equation (6), the voltage equations in the $dq0$ coordinate system can be obtained as:

$$\begin{bmatrix} u_{ld} \\ u_{lq} \\ u_{l0} \end{bmatrix} = R \begin{bmatrix} i_{ld} \\ i_{lq} \\ i_{l0} \end{bmatrix} + \begin{bmatrix} L+M & 0 & 0 \\ 0 & L+M & 0 \\ 0 & 0 & L-2M \end{bmatrix} \frac{d}{dt} \begin{bmatrix} i_{ld} \\ i_{lq} \\ i_{l0} \end{bmatrix} + \begin{bmatrix} 0 & -\omega(L+M) & 0 \\ \omega(L+M) & 0 & 0 \\ 0 & 0 & 0 \end{bmatrix} \begin{bmatrix} i_{ld} \\ i_{lq} \\ i_{l0} \end{bmatrix} \tag{7}$$

where u_{ld}, u_{lq}, and u_{l0} and i_{ld}, i_{lq}, and i_{l0} are the d-axis, q-axis, and zero-sequence components of the three-phase voltages and currents of the TCI, respectively.

As can be seen from Equation (7), the TCI has low zero-sequence inductance and large dq axes inductances, which is conducive to the fast dynamic response of the zero-sequence current in the TCI and reduced power loss [21]. Meanwhile, by focusing on the zero-sequence equation in Equation (7), it can be seen that the zero-sequence current in the TCI is directly dependent on the ZSV applied to the TCI. Thus, the necessary keys to realize the voltage balance between the bipolar DC ports of the TCIBAR are the control and accurate generation of the ZSV.

3. Proposed DPC Based on Optimized Sector Division

3.1. Extension of Voltage Vector

In the DPC-based control architecture, the hysteresis power control of the rectifier can be implemented based on a pre-established switching table, and the switching table directly affects the control performance of the DPC strategy. The establishment of the switching table is a critical step in developing a DPC strategy. In the classic DPC for unipolar output rectifiers, the establishment of a switching table only needs to consider the effect of voltage vectors on the power variation. However, for the TCIBAR, the voltage vector not only determines the power variation of the converter, but it also affects the voltage balance between the bipolar DC ports. Therefore, to establish an appropriate switching table for the DPC of TCIBAR, the effects of the voltage vectors on both the power variation rate and the ZSV need to be analyzed.

According to the power model in Equation (5), the relationship between the voltage vector and the power variation rate can be obtained by representing the VSC voltages (u_d and u_q) with the switching functions of voltage vectors, as shown in Equation (8),

$$\begin{cases} \frac{dp}{dt} = \frac{e_d}{L_s}(-S_d U_{dc} + e_d) \\ \frac{dq}{dt} = \frac{e_d}{L_s} S_q U_{dc} \end{cases} \tag{8}$$

where S_d and S_q are the switching functions in the $dq0$ coordinate system.

Meanwhile, since the three-phase voltages of the TCI can be expressed as Equation (9), the ZSV u_{I0} of the TCI can be calculated based on the Park transformation, as shown in Equation (10),

$$\begin{cases} u_{aN} = S_a U_{dc} - \eta U_{dc} \\ u_{bN} = S_b U_{dc} - \eta U_{dc} \\ u_{cN} = S_c U_{dc} - \eta U_{dc} \end{cases} \tag{9}$$

$$u_{I0} = S_0 U_{dc} - \sqrt{3}\eta U_{dc} \tag{10}$$

where η is the voltage coefficient of the DC side neutral point.

As Equations (8) and (10) show, the effect of the voltage vectors can be analyzed based on the switching functions in the $dq0$ coordinate system, which can be deduced as follows:

$$\begin{bmatrix} S_d \\ S_q \\ S_0 \end{bmatrix} = \sqrt{\frac{2}{3}} \begin{bmatrix} \cos\omega t & \cos(\omega t - \frac{2}{3}\pi) & \cos(\omega t + \frac{2}{3}\pi) \\ -\sin\omega t & -\sin(\omega t - \frac{2}{3}\pi) & -\sin(\omega t + \frac{2}{3}\pi) \\ \frac{1}{\sqrt{2}} & \frac{1}{\sqrt{2}} & \frac{1}{\sqrt{2}} \end{bmatrix} \begin{bmatrix} S_a \\ S_b \\ S_c \end{bmatrix} \tag{11}$$

where S_x ($x = a, b, c$) are the switching states of the three-phase bridges in TCIBAR.

By substituting the switching states of the basic voltage vectors ($\boldsymbol{V}_0$–$\boldsymbol{V}_7$) into Equation (11), the switching functions of the basic voltage vector are obtained, as shown in Table 1.

Table 1. The switching functions of basic voltage vectors.

Vectors	S_a	S_b	S_c	S_d	S_q	S_0
$\boldsymbol{V}_0$	0	0	0	0	0	0
$\boldsymbol{V}_1$	1	0	0	$\sqrt{\frac{2}{3}}\cos\omega t$	$-\sqrt{\frac{2}{3}}\sin\omega t$	$\frac{1}{\sqrt{3}}$
$\boldsymbol{V}_2$	1	1	0	$\sqrt{\frac{2}{3}}\cos(\omega t - \frac{\pi}{3})$	$-\sqrt{\frac{2}{3}}\sin(\omega t - \frac{\pi}{3})$	$\frac{2}{\sqrt{3}}$
$\boldsymbol{V}_3$	0	1	0	$\sqrt{\frac{2}{3}}\cos(\omega t - \frac{2\pi}{3})$	$-\sqrt{\frac{2}{3}}\sin(\omega t - \frac{2\pi}{3})$	$\frac{1}{\sqrt{3}}$
$\boldsymbol{V}_4$	0	1	1	$-\sqrt{\frac{2}{3}}\cos\omega t$	$\sqrt{\frac{2}{3}}\sin\omega t$	$\frac{2}{\sqrt{3}}$
$\boldsymbol{V}_5$	0	0	1	$\sqrt{\frac{2}{3}}\cos(\omega t + \frac{2\pi}{3})$	$-\sqrt{\frac{2}{3}}\sin(\omega t + \frac{2\pi}{3})$	$\frac{1}{\sqrt{3}}$
$\boldsymbol{V}_6$	1	0	1	$\sqrt{\frac{2}{3}}\cos(\omega t + \frac{\pi}{3})$	$-\sqrt{\frac{2}{3}}\sin(\omega t + \frac{\pi}{3})$	$\frac{2}{\sqrt{3}}$
$\boldsymbol{V}_7$	1	1	1	0	0	$\sqrt{3}$

It can be seen from Table 1 that basic voltage vectors have different zero-sequence switching functions S_0, which leads to differences in the ZSV components in basic voltage vectors. Therefore, if the basic voltage vectors are directly adopted to establish the switching table for hysteresis power control, regardless of its effect on the ZSV, the zero-sequence current in TCI will be uncontrollable, which will lead to voltage imbalance between the bipolar DC ports of the TCIBAR. In the meantime, due to the limited number of basic voltage vectors in TCIBAR, there are not enough redundant voltage vectors that can be selected to realize hysteresis power control while maintaining the voltage balance between the bipolar DC ports. To overcome this problem, a simple and effective solution is to extend the basic voltage vectors and find new voltage vectors that have the same ZSV component to establish the switching table for the TCIBAR.

In this paper, a set of new voltage vectors are synthesized to extend the eight basic voltage vectors, as shown in Figure 2. Figure 2 shows that the new voltage vectors ($\boldsymbol{U}_1$–$\boldsymbol{U}_6$) can be synthesized by the adjacent non-zero basic voltage vectors, and the adjacent non-zero basic voltage vectors each act for half of one control cycle. In addition, the equivalent switching states of the synthesized voltage vectors can be represented by 0, 0.5, and 1. Similarly, the switching functions of the synthesized voltage vectors can be deduced as shown in Table 2.

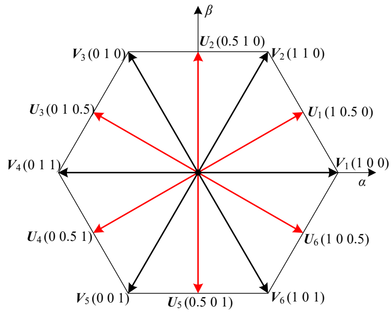

Figure 2. The synthesized voltage vectors.

Table 2. The switching functions of the synthesized voltage vectors.

Vectors	S_a	S_b	S_c	S_d	S_q	S_0
$\boldsymbol{U}_1$	1	0.5	0	$\frac{1}{\sqrt{2}}\cos(\omega t-\frac{\pi}{6})$	$-\frac{1}{\sqrt{2}}\sin(\omega t-\frac{\pi}{6})$	$\frac{\sqrt{3}}{2}$
$\boldsymbol{U}_2$	0.5	1	0	$\frac{1}{\sqrt{2}}\cos(\omega t-\frac{\pi}{2})$	$-\frac{1}{\sqrt{2}}\sin(\omega t-\frac{\pi}{2})$	$\frac{\sqrt{3}}{2}$
$\boldsymbol{U}_3$	0	1	0.5	$\frac{1}{\sqrt{2}}\cos(\omega t-\frac{5}{6}\pi)$	$-\frac{1}{\sqrt{2}}\sin(\omega t-\frac{5}{6}\pi)$	$\frac{\sqrt{3}}{2}$
$\boldsymbol{U}_4$	0	0.5	1	$\frac{1}{\sqrt{2}}\cos(\omega t+\frac{5}{6}\pi)$	$-\frac{1}{\sqrt{2}}\sin(\omega t+\frac{5}{6}\pi)$	$\frac{\sqrt{3}}{2}$
$\boldsymbol{U}_5$	0.5	0	1	$\frac{1}{\sqrt{2}}\cos(\omega t+\frac{\pi}{2})$	$-\frac{1}{\sqrt{2}}\sin(\omega t+\frac{\pi}{2})$	$\frac{\sqrt{3}}{2}$
$\boldsymbol{U}_6$	1	0	0.5	$\frac{1}{\sqrt{2}}\cos(\omega t+\frac{\pi}{6})$	$-\frac{1}{\sqrt{2}}\sin(\omega t+\frac{\pi}{6})$	$\frac{\sqrt{3}}{2}$

As Table 2 shows, the synthesized voltage vectors have the same zero-sequence switching function S_0; thus, the ZSV components in the synthesized voltage vectors are all the same, according to Equation (10). Meanwhile, when the DC voltages of the bipolar DC ports are balanced (that is, η = 0.5), the ZSV applied to the TCI will be equal to zero under the action of the synthesized voltage vectors. Therefore, if the synthesized voltage vectors are used to establish the switching table, the TCIBAR can realize hysteresis power control without causing the runaway of the zero-sequence current in the TCI.

3.2. Effect of Voltage Vector on Power Variation

In order to establish a feasible switching table for TCIBAR, the effects of the synthesized voltage vectors on the power variation were analyzed quantitatively, and the area divisions of vector space for active and reactive power were obtained.

3.2.1. Vector Space Division for Reactive Power

According to the power model in Equation (8), since L_s, U_{dc}, and e_d are always positive, the sign of the reactive power variation rate (dq/dt) is directly dependent on the switching function S_q.

Take the synthesized voltage vector $\boldsymbol{U}_1$ as an example and substitute its switching function S_q into the expression of dq/dt to get the following equation:

$$\frac{dq}{dt}=-\frac{e_d U_{dc}}{\sqrt{2}L_s}\sin(\omega t-\frac{\pi}{6}) \tag{12}$$

By analyzing the value range of Equation (12), the following results can be obtained: if $\pi/6<\omega t<7\pi/6$, $dq/dt<0$, and if $-5\pi/6<\omega t<\pi/6$, $dq/dt>0$.

Therefore, the vector space is now evenly divided into two areas with the boundaries of $\omega t=\pi/6$ and $\omega t=7\pi/6$, in which the signs of dq/dt are opposite. When the AC source voltage vector is in these two areas, the synthesized voltage vector $\boldsymbol{U}_1$ has the opposite effect on the reactive power of the TCIBAR.

Then, the switching functions S_q of the other voltage vectors are successively substituted into the expression of dq/dt in Equation (8), and the areas divided by different voltage vectors' effect on reactive power can be obtained, as shown in Figure 3.

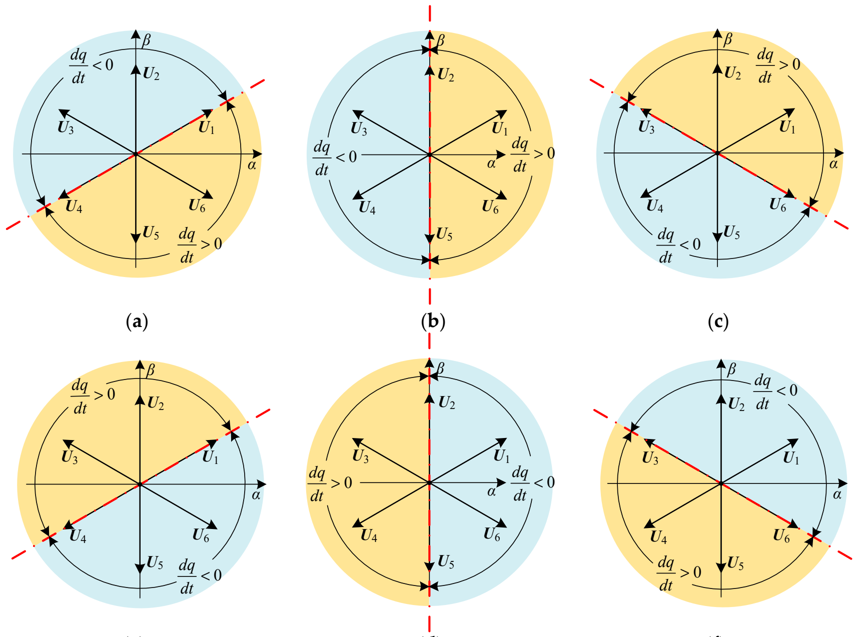

Figure 3. Illustration of areas divided by the synthesized voltage vectors' effect on reactive power. (**a**) $\boldsymbol{U}_1$, (**b**) $\boldsymbol{U}_2$, (**c**) $\boldsymbol{U}_3$, (**d**)$\boldsymbol{U}_4$, (**e**) $\boldsymbol{U}_5$, and (**f**) $\boldsymbol{U}_6$.

Based on the effect of the six synthesized voltage vectors on reactive power in Figure 3, the vector space can be divided into six equal areas, as shown in Figure 4.

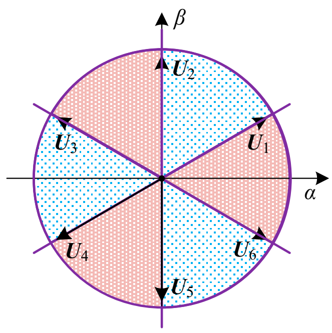

Figure 4. Vector space division for reactive power.

3.2.2. Vector Space Division for Active Power

The sign of active power variation rate (dp/dt) is determined by $-S_d + e_d/U_{dc}$, which is different from reactive power and not only depends on the switching function S_d, but is also related to the amplitude of the AC source voltage e_d and the DC bus voltage U_{dc}. Therefore, by analyzing the value of $-S_d + e_d/U_{dc}$ corresponding to each synthesized voltage vector, the vector space division for active power can be obtained.

Similarly, taking the synthesized voltage vector $\boldsymbol{U}_1$ as an example and substituting its switching function S_d into $-S_d + e_d/U_{dc}$, the following expression is obtained:

$$-S_d + \frac{e_d}{U_{dc}} = -\frac{1}{\sqrt{2}}[\cos(\omega t - \frac{\pi}{6}) - \frac{e_d}{U_{dc}/\sqrt{2}}] \tag{13}$$

where $U_{dc}/\sqrt{2}$ is the amplitude of the synthesized voltage vector under the condition of constant power coordinate transformation, denoted as $|U_m|$.

Since $0 < e_d/|U_m| \leq 1$, $e_d/|U_m|$ can be regarded as the cosine of the angle δ in the first quadrant, or $\cos\delta = e_d/|U_m|$, then Equation (13) can be rewritten as:

$$-S_d + \frac{e_d}{U_{dc}} = -\frac{1}{\sqrt{2}}[\cos(\omega t - \frac{\pi}{6}) - \cos\delta] = \sqrt{2}\sin(\frac{\omega t - \frac{\pi}{6} + \delta}{2})\sin(\frac{\omega t - \frac{\pi}{6} - \delta}{2}) \quad (14)$$

As Equation (14) shows, when $\sin[(\omega t - \pi/6 + \delta)/2]$ and $\sin[(\omega t - \pi/6 - \delta)/2]$ have opposite signs, $-S_d + e_d/U_{dc}$ is negative, and the active power of TCIBAR decreases. When the signs are the same, $-S_d + e_d/U_{dc}$ is positive, and the active power increases. Therefore, the vector space is divided into two unequal areas with $\omega t = \pi/6 \pm \delta$ as the boundaries, and the boundaries will change with the angle δ, which can be calculated by the arccosine of $e_d/|U_m|$. When the AC source voltage vector is in these two areas, the active power of the TCIBAR changes in opposite directions under the action of $\boldsymbol{U}_1$. As shown in Figure 5, the vector space division for active power under the action of other synthesized voltage vectors can be deduced using the same method, and the boundaries can be expressed as:

$$\omega t = \frac{\pi}{6} \pm \delta + \frac{\pi}{3}(m-1), \qquad m = 1,\ 2,\ 3, \cdots, 6 \quad (15)$$

where m = 1, . . . , 6 correspond to the boundaries of voltage vectors $\boldsymbol{U}_1$, $\boldsymbol{U}_2$, $\boldsymbol{U}_3$, $\boldsymbol{U}_4$, $\boldsymbol{U}_5$, and $\boldsymbol{U}_6$, respectively.

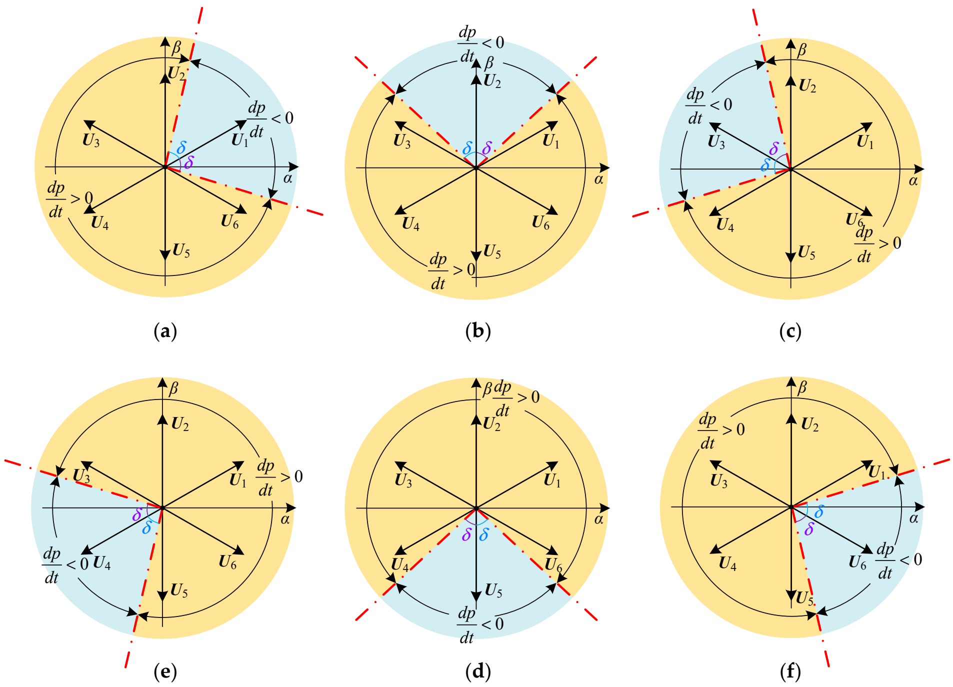

Figure 5. Illustration of areas divided by the synthesized voltage vectors' effect on active power. **(a)** $\boldsymbol{U}_1$, **(b)** $\boldsymbol{U}_2$, **(c)**$\boldsymbol{U}_3$, **(d)**$\boldsymbol{U}_4$, **(e)**$\boldsymbol{U}_5$, and **(f)** $\boldsymbol{U}_6$.

By overlapping the different area divisions in Figure 5, the whole vector space can be divided into twelve unequal areas, as shown in Figure 6.

3.3. Optimized Sector Division and Switching Table

By combining the vector space divisions in Figures 4 and 6, an optimized sector division based on the effect of synthesized voltage vectors on power variation can be obtained, as shown in Figure 7, and the sector division is different when angle δ changes.

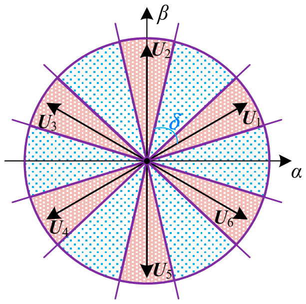

Figure 6. Vector space division for active power.

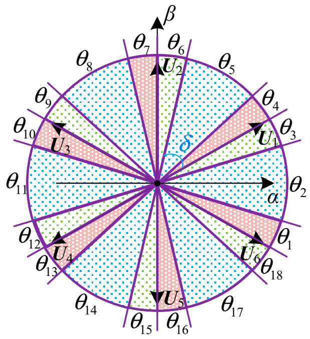

Figure 7. The optimized sector division proposed in this paper.

Compared with the traditional 12-sector division, the proposed sector division method divides the vector space into 18 sectors, which optimizes the sector division accuracy and can ensure the correct effect of the synthesized voltage vectors on the power variation in each sector. In addition, when angle δ is equal to $\pi/6$ or $\pi/2$, the optimized 18-sector division degenerates into the traditional 12-sector division. Thus, the traditional 12-sector division is a special case of optimized sector division.

Based on the optimized 18-sector division and the synthesized voltage vectors, a novel switching table for the DPC of TCIBAR can be established. Meanwhile, to facilitate the experimental comparison used in the next section, a switching table based on the traditional 12-sector division is also established by qualitatively analyzing the effect of the new synthesized voltage vectors on the power variation of TCIBAR based on the space vector diagram [33,34]. Tables 3 and 4 represent the switching tables based on the 12-sector division and the 18-sector division, respectively, where s_P and s_Q are the outputs of the active and reactive hysteresis comparators.

Table 3. Switching table based on the traditional 12-sector division.

s_P	s_Q	θ_1	θ_2	θ_3	θ_4	θ_5	θ_6	θ_7	θ_8	θ_9	θ_{10}	θ_{11}	θ_{12}
0	0	U_6	U_6	U_1	U_1	U_2	U_2	U_3	U_3	U_4	U_4	U_5	U_5
0	1	U_1	U_1	U_2	U_2	U_3	U_3	U_4	U_4	U_5	U_5	U_6	U_6
1	0	U_4	U_5	U_5	U_6	U_6	U_1	U_1	U_2	U_2	U_3	U_3	U_4
1	1	U_2	U_3	U_3	U_4	U_4	U_5	U_5	U_6	U_6	U_1	U_1	U_2

Table 4. Switching table based on the optimized 18-sector division.

s_P	s_Q	θ_1	θ_2	θ_3	θ_4	θ_5	θ_6	θ_7	θ_8	θ_9	θ_{10}	θ_{11}	θ_{12}	θ_{13}	θ_{14}	θ_{15}	θ_{16}	θ_{17}	θ_{18}
0	0	U_6	U_6	U_6	U_1	U_1	U_1	U_2	U_2	U_2	U_3	U_3	U_3	U_4	U_4	U_4	U_5	U_5	U_5
0	1	U_1	U_1	U_1	U_2	U_2	U_2	U_3	U_3	U_3	U_4	U_4	U_4	U_5	U_5	U_5	U_6	U_6	U_6
1	0	U_5	U_5	U_6	U_6	U_6	U_1	U_1	U_1	U_2	U_2	U_2	U_3	U_3	U_3	U_4	U_4	U_4	U_5
1	1	U_1	U_2	U_2	U_2	U_3	U_3	U_3	U_4	U_4	U_4	U_5	U_5	U_5	U_6	U_6	U_6	U_1	U_1

3.4. Voltage Balance Control under DPC Architecture

As analyzed in Section 2, the ZSV applied to the TCI plays a vital role in the voltage balance control between the bipolar DC ports of TCIBAR. Meanwhile, the control of ZSV can be divided into two parts: the acquisition of the reference value and the generation of the actual value.

First, to obtain the reference ZSV, a double closed-loop control algorithm is designed, in which the control objects of the outer and inner loops are the voltage difference Δu between the bipolar DC ports and the zero-sequence current in TCI, respectively. Proportional–integral (PI) regulators can be used to eliminate errors and calculate the reference value of the ZSV.

However, due to the lack of voltage modulation module in DPC, the accurate generation of the actual ZSV is a primary challenge to realize the voltage balance control of TCIBAR. Therefore, this subsection focuses on the generation of ZSV, and a ZSV generation method under DPC architecture is studied.

To achieve the accurate generation of ZSV, the ZSV components in different voltage vectors need to be analyzed. By substituting the zero-sequence switching functions S_0 of the synthesized voltage vectors into Equation (10), the ZSV components in the synthesized voltage vectors are all equal to $\sqrt{3}(1-2\eta)U_{dc}/2$. The required ZSV cannot be accurately generated only by the six synthesized voltage vectors.

According to the volt-second equivalent principle, a feasible ZSV generation method is to find another appropriate voltage vector that has a different ZSV component and insert it into the synthesized voltage vector with a proper duration time in one control cycle, which generates the ZSV without greatly impacting the power control. When looking back to the basic voltage vectors, the ZSV components in the zero vectors $\boldsymbol{V}_0$ and $\boldsymbol{V}_7$ are $-\sqrt{3}\eta U_{dc}$ and $\sqrt{3}(1-\eta)U_{dc}$, respectively. Due to the constraint $0 < \eta < 1$, the signs of $-\sqrt{3}\eta U_{dc}$ and $\sqrt{3}(1-\eta)U_{dc}$ are opposite. Meanwhile, the ZSV components in $\boldsymbol{V}_0$, $\boldsymbol{V}_7$, and the synthesized voltage vector always satisfy the following inequality:

$$-\sqrt{3}\eta U_{dc} < \sqrt{3}(1-2\eta)U_{dc}/2 < \sqrt{3}(1-\eta)U_{dc} \tag{16}$$

In addition, since the zero vectors have a weak influence on the power control of TCIBAR, $\boldsymbol{V}_0$ and $\boldsymbol{V}_7$ can be inserted into the synthesized voltage vector to generate the desired ZSV.

If the reference value of ZSV (u_{l0}^*) is less than $\sqrt{3}(1-2\eta)U_{dc}/2$, the zero vector $\boldsymbol{V}_0$ is inserted. In this case, the action time of voltage vectors in one control cycle can be calculated as:

$$\begin{cases} u_{l0}^* T_s = \frac{\sqrt{3}(1-2\eta)}{2} U_{dc} t_m - \sqrt{3}\eta U_{dc} t_0 \\ t_m + t_0 = T_s \end{cases} \tag{17}$$

where t_m and t_0 are the action time of the synthesized voltage vector and $\boldsymbol{V}_0$, respectively.

If the reference value of ZSV (u_{l0}^*) is greater than $\sqrt{3}(1-2\eta)U_{dc}/2$, the zero vector $\boldsymbol{V}_7$ is inserted. In this case, the action time of voltage vectors can be calculated as:

$$\begin{cases} u_{l0}^* T_s = \frac{\sqrt{3}(1-2\eta)}{2} U_{dc} t_m + \sqrt{3}(1-\eta) U_{dc} t_7 \\ t_m + t_7 = T_s \end{cases} \tag{18}$$

where t_7 is the action time of $\boldsymbol{V}_7$.

Thus, by comparing the values of $\sqrt{3}(1-2\eta)U_{dc}/2$ and u_{l0}^*, the inserted zero vector and its action time can be determined. On this basis, the voltage balance control between the bipolar DC ports of the TCIBAR can be realized under the DPC architecture.

Finally, based on the above analysis and research in this section, the complete DPC strategy based on an optimized sector division can be built for the TCIBAR, and the control diagram is shown in Figure 8.

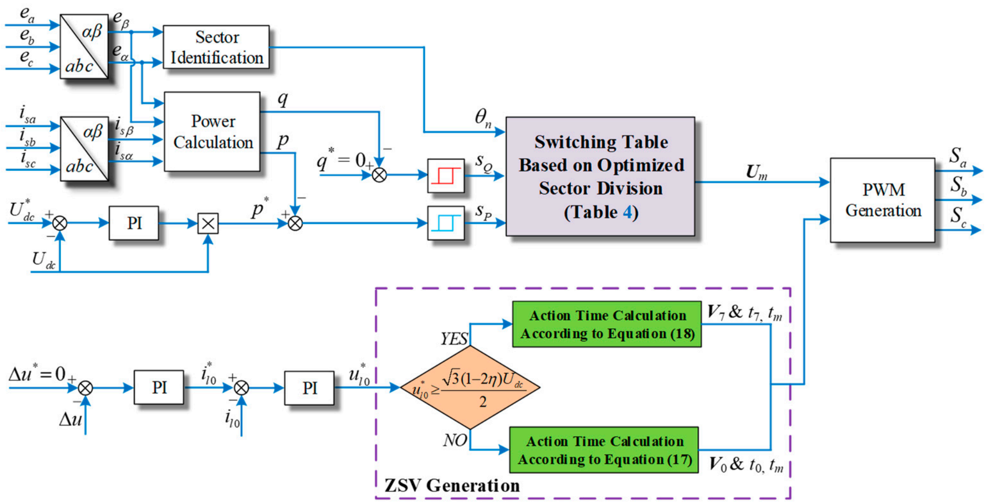

Figure 8. Control diagram of the proposed DPC strategy for TCIBAR.

4. Experimental Results

4.1. Experimental Parameters

To verify the feasibility and research the performance of the proposed DPC strategy, an experimental platform of TCIBAR was built in the laboratory. The schematic of the experimental platform is shown in Figure 9, and the experimental parameters are listed in Table 5. In the experimental platform, the sampling frequency of the digital signal processor was set to 20 kHz, and the control cycle T_s was equal to 50 µs.

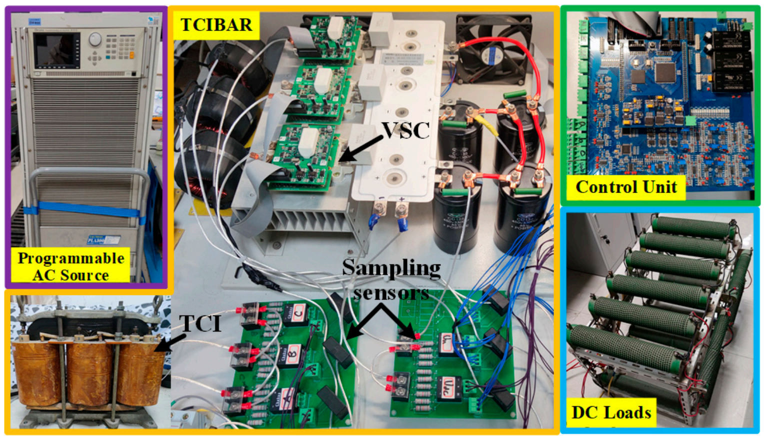

Figure 9. Experimental platform of the TCIBAR.

Table 5. Parameters of the experimental platform.

Parameter	Symbol	Value
Rated power	P	5 kW
RMS value of AC source phase voltage	E_{ac}	115 V
Frequency of AC source	f_{ac}	400 Hz
Rated DC bus voltage	U_{dc}	360 V
Rated positive voltage	u_p	180 V
Rated negative voltage	u_n	180 V
Positive port capacitance	C_p	6600 µF
Negative port capacitance	C_n	6600 µF
Filter inductance	L_s	1.5 mH
Self-inductance of TCI	L	0.526 H
Mutual inductance of TCI	M	0.259 H

4.2. Steady State Experimental Study

First, to prove the feasibility and effectiveness of the proposed DPC strategy, the comparison experiments analyzed the classic and proposed DPC strategies under no load, balanced load, and unbalanced load conditions. The control diagram of the classic DPC is presented in [25], in which only the basic voltage vectors were used to establish the switching table based on the traditional 12-sector division, and the voltage balance control was not included.

Figure 10 shows the experimental results of different DPC strategies under a no load condition. As can be seen from Figure 10a, since the classic DPC does not involve the zero-sequence component control as well as the voltage balance control, a large fluctuation occurred in the total zero-sequence current i_{ln}, and the voltages of the bipolar DC ports (u_p and u_n) were not balanced. The proposed DPC strategy effectively controlled the zero-sequence current and stabilized i_{ln} at 0, as shown in Figure 10b. Meanwhile, the voltage balance between the bipolar DC ports was realized under the no load condition.

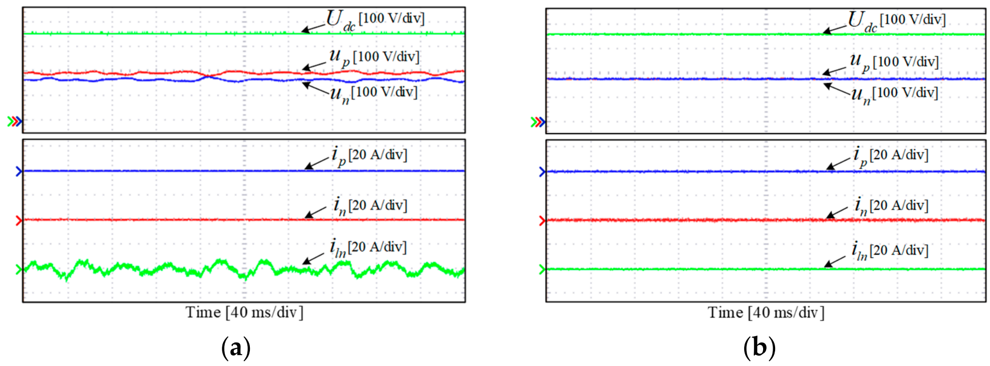

Figure 10. Experimental results of different DPC strategies under a no load condition. (**a**) Classic DPC strategy and (**b**) proposed DPC strategy.

The experimental results of different DPC strategies under a balanced load condition are shown in Figure 11. In the balanced load condition, both the positive and negative ports of the TCIBAR were loaded with 13.3 Ω resistors. Figure 11a shows that although the bipolar DC voltages were balanced by the balanced loads, the zero-sequence current ripple of the classic DPC was larger than that of the proposed DPC strategy, which was caused by the different ZSV components in the basic voltage vectors. Thus, based on the new synthesized voltage vectors, the proposed DPC strategy reduced the zero-sequence current ripple in the TCIBAR, as shown in Figure 11b.

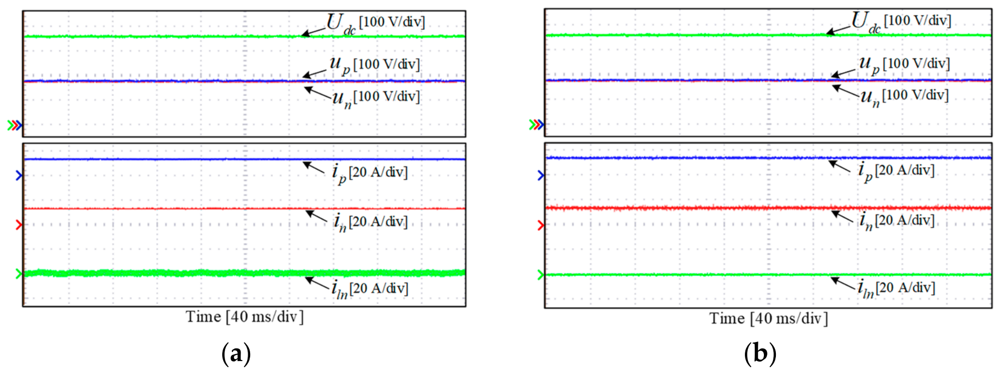

Figure 11. Experimental results of different DPC strategies under a balanced load condition. (**a**) Classic DPC strategy and (**b**) proposed DPC strategy.

Figure 12 shows the experimental results of the classic and proposed DPC strategies under an unbalanced load condition, where only the negative port of the TCIBAR was loaded with a 13.3 Ω resistor, and the positive port was kept unloaded. As shown in Figure 12a, when the classic DPC was employed under an unbalanced load condition, the total zero-sequence current i_{ln} was almost out of control, and the voltages of the positive and negative ports fluctuated greatly and could not maintain balance. As Figure 12b shows, based on the proposed DPC strategy, the total zero-sequence current i_{ln} was controlled to provide the unbalanced current for the negative port. Meanwhile, the voltage fluctuations of the bipolar DC ports were suppressed, and the voltage balance between the bipolar DC ports was realized, even under an unbalanced load condition.

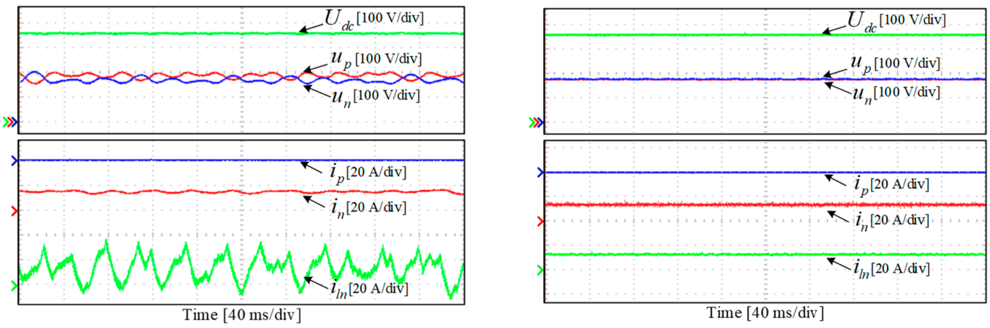

(**a**) (**b**)

Figure 12. Experimental results of different DPC strategies under an unbalanced load condition. (**a**) Classic DPC strategy and (**b**) proposed DPC strategy.

Therefore, according to the above experimental results, the feasibility and effectiveness of the proposed DPC strategy were validated. In addition, to better illustrate the performance improvement created by the optimized sector division method, the switching tables based on the traditional 12-sector division (Table 3) and the optimized 18-sector division (Table 4) were comparatively tested. The experimental results based on the traditional 12-sector division and the optimized 18-sector division are shown in Figures 13 and 14, respectively.

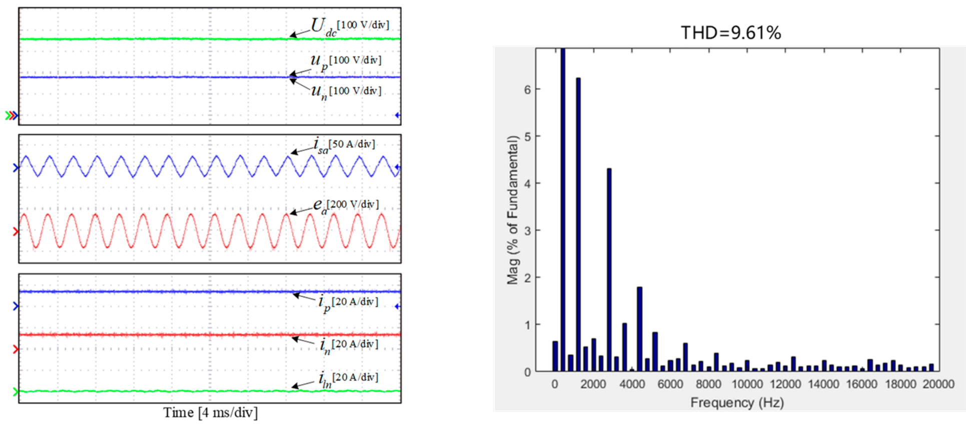

(**a**) (**b**)

Figure 13. Experimental results based on the traditional 12-sector division. (**a**) Voltage and current waveforms of TCIBAR and (**b**) fast Fourier transform (FFT) results of the phase current.

As Figures 13a and 14a display, both switching tables based on the 12-sector division and the 18-sector division realized the effective control of the bipolar DC voltages and the total DC bus voltage. Meanwhile, the total zero-sequence current i_{ln} was stably maintained at 0 A. In addition, when compared with the experimental results in Figure 13b, the total harmonic distortion (THD) of the phase current in Figure 14b reduced from 9.61% to 6.95% when the switching table based on the optimized 18-sector division was used. Therefore, the optimized sector division method improved the quality of the phase currents in the TCIBAR and had better steady-state performance, which created the advantage of a lower filter weight and was beneficial to the application of the TCIBAR in MEA.

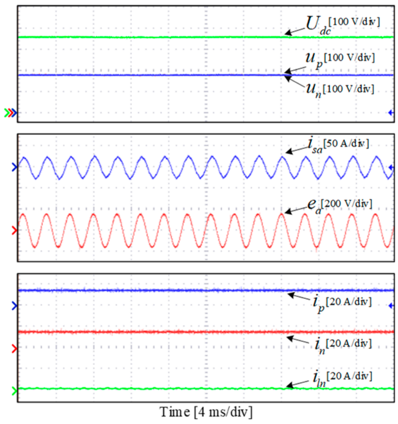

(**a**)

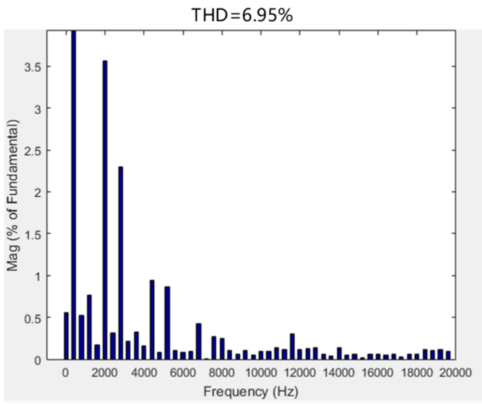

(**b**)

Figure 14. Experimental results based on the optimized 18-sector division. (**a**) Voltage and current waveforms of TCIBAR and (**b**) fast Fourier transform (FFT) results of the phase current.

4.3. Dynamic Experimental Study

To study the dynamic performance of the proposed DPC strategy, load step experiments were done under balanced and unbalanced load conditions, and the load conditions were the same as those described above. The load step experimental results under balanced and unbalanced load conditions are shown in Figures 15 and 16, respectively.

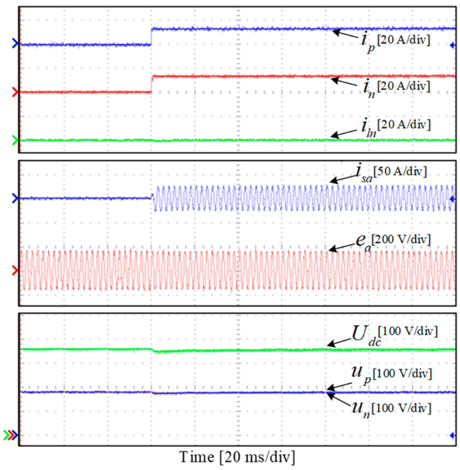

Figure 15. Load step experimental results under a balanced load condition.

It can be seen from Figures 15 and 16 that the proposed DPC strategy achieved a fast dynamic response under both the balanced and unbalanced load conditions, and the phase currents of the TCIBAR increased rapidly to provide the required load power after the step loads were switched on.

As shown in Figure 15, the voltage drop caused by the balanced step loads was immediately eliminated, and the dynamic process took about 20 ms. In the meantime, the total zero-sequence current i_{ln} was stabilized at 0 A, and the voltage balance between the bipolar DC ports was maintained during the dynamic process. Different from the balanced step load, the unbalanced step load led to a voltage imbalance between the bipolar DC ports, as shown in Figure 16. Based on the proposed strategy, the TCIBAR actively regulated the zero-sequence current, and the voltage balance between the bipolar DC ports was restored in 30 ms.

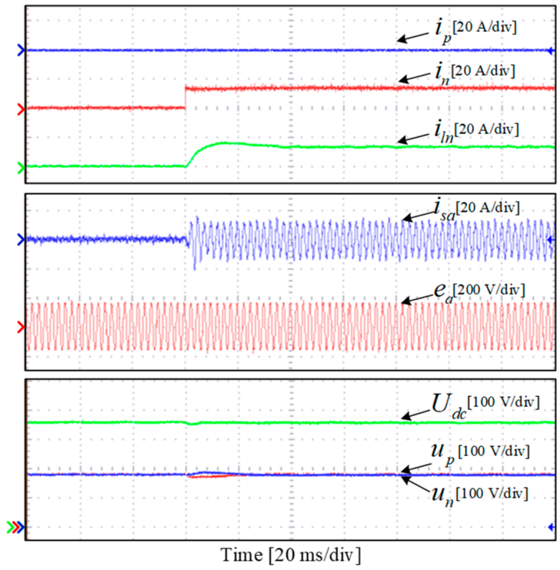

Figure 16. Load step experimental results under an unbalanced load condition.

5. Conclusions

In this paper, a DPC strategy based on optimized sector division was proposed for the TCIBAR applied in MEA. The feasibility and effectiveness of the proposed DPC strategy were proven by steady state and dynamic research using an experimental platform. The following conclusions were obtained:

1. Based on the instantaneous power theory, the power model of the TCIBAR in the synchronous rotating coordinate system was established and verified.
2. Based on the new synthesized voltage vectors, the proposed DPC strategy realized the hysteresis power control of TCIBAR without causing the runaway of the zero-sequence current in TCI.
3. The optimized sector division method in the proposed DPC strategy effectively reduced the THD of the phase currents and improved the steady-state performance of the TCIBAR.
4. Based on the proposed ZSV generation method, the proposed DPC strategy realized the voltage balance control of the bipolar DC ports in TCIBAR and maintained the voltage balance between the bipolar DC ports, even under unbalanced load conditions.

In the future, to improve the adaptability of the TCIBAR to the actual generators in MEAs, the authors will further study the performance of the proposed DPC strategy under the condition of non-ideal AC sources.

Author Contributions: Conceptualization, Y.Z.; methodology, Y.Z.; software, Y.Z.; validation, Y.Z.; formal analysis, Y.Z. and F.B.; investigation, Y.Z.; resources, Y.Z., W.H. and F.B.; data curation, Y.Z.; writing—original draft preparation, Y.Z.; writing—review and editing, Y.Z. and F.B.; visualization, Y.Z., W.H. and F.B.; supervision, W.H. and F.B.; project administration, W.H.; funding acquisition, F.B. All authors have read and agreed to the published version of the manuscript.

Funding: This research was funded by the National Natural Science Foundation of China under Grant 52177050.

Data Availability Statement: Not applicable.

Conflicts of Interest: The authors declare no conflict of interest.

Abbreviations

DPC	Direct power control
MEA	More electric aircraft
TCIBAR	Three-phase coupled inductor-based bipolar output active rectifier
TCI	Three-phase coupled inductor
ZSV	Zero-sequence voltage
EPS	Electrical power system
HVDC	High-voltage direct current
ATRU	Auto transformer rectifier unit
VSC	Voltage source converter
VOC	Voltage-oriented control
PI	Proportional–integral
FFT	Fast Fourier transform
THD	Total harmonic distortion

References

1. Barzkar, A.; Ghassemi, M. Electric power systems in more and all electric aircraft: A review. *IEEE Access* **2020**, *8*, 169314–169332. [CrossRef]
2. Sayed, E.; Abdalmagid, M.; Pietrini, G.; Sa'adeh, N.M.; Callegaro, A.D.; Goldstein, C.; Emadi, A. Review of electric machines in more-/hybrid-/turbo-electric aircraft. *IEEE Trans. Transp. Electrif.* **2021**, *7*, 2976–3005. [CrossRef]
3. Weng, L.; Zhang, X.; Yao, T.; Bu, F.; Li, H. A thrust cooperative control strategy of multiple propulsion motors for distributed electric propulsion aircraft. *World Electr. Veh. J.* **2021**, *12*, 199. [CrossRef]
4. Rajashekara, K. Power conversion technologies for automotive and aircraft systems. *IEEE Electrif. Mag.* **2014**, *2*, 50–60. [CrossRef]
5. Chen, W.; Li, S.; Sun, W.; Bi, K.; Lin, Z.; Zhang, G. Wide frequency PWM rectifier control system based on improved deadbeat direct power control. *World Electr. Veh. J.* **2022**, *13*, 230. [CrossRef]
6. Patnaik, B.; Kumar, S.; Gawre, S. Recent advances in converters and storage technologies for more electric aircrafts: A review. *IEEE J. Miniat. Air Space Syst.* **2022**, *3*, 78–87. [CrossRef]
7. Roboam, X.; Sareni, B.; Andrade, A.D. More electricity in the air: Toward optimized electrical networks embedded in more-electrical aircraft. *IEEE Ind. Electron. Mag.* **2012**, *6*, 6–17. [CrossRef]
8. Wheeler, P. Technology for the more and all electric aircraft of the future. In Proceedings of the 2016 IEEE International Conference on Automatica (ICA–ACCA), Curico, Chile, 19–21 October 2016.
9. Lang, X.; Yang, T.; Enalou, H.B.; Bozhko, S.; Wheeler, P. An enhanced power generation centre for more electric aircraft applications. In Proceedings of the 2018 IEEE International Conference on Electrical Systems for Aircraft, Railway, Ship Propulsion and Road Vehicles & International Transportation Electrification Conference (ESARS-ITEC), Nottingham, UK, 7–9 November 2018.
10. Sarlioglu, B.; Morris, C.T. More electric aircraft: Review, challenges, and opportunities for commercial transport aircraft. *IEEE Trans. Transp. Electrif.* **2015**, *1*, 54–64. [CrossRef]
11. Schefer, H.; Fauth, L.; Kopp, T.H.; Mallwitz, R.; Friebe, J.; Kurrat, M. Discussion on electric power supply systems for all electric aircraft. *IEEE Access* **2020**, *8*, 84188–84216. [CrossRef]
12. Chen, J.W.; Wang, C.; Chen, J. Investigation on the selection of electric power system architecture for future more electric aircraft. *IEEE Trans. Transp. Electrif.* **2018**, *4*, 563–576. [CrossRef]
13. Lei, T.; Min, Z.; Gao, Q.; Song, L.; Zhang, X.; Zhang, X. The architecture optimization and energy management technology of aircraft power systems: A review and future trends. *Energies* **2022**, *15*, 4109. [CrossRef]
14. Madonna, V.; Giangrande, P.; Galea, M. Electrical power generation in aircraft: Review, challenges, and opportunities. *IEEE Trans. Transp. Electrif.* **2018**, *4*, 646–659. [CrossRef]
15. Karanayil, B.; Ciobotaru, M.; Agelidis, V.G. Power flow management of isolated multiport converter for more electric aircraft. *IEEE Trans. Power Electron.* **2017**, *32*, 5850–5861. [CrossRef]
16. Buticchi, G.; Bozhko, S.; Liserre, M.; Wheeler, P.; Al-Haddad, K. On-board microgrids for the more electric aircraft–Technology review. *IEEE Trans. Ind. Electron.* **2019**, *66*, 5588–5599. [CrossRef]
17. Yang, T.; Bozhko, S.; Wheeler, P.; Wang, S.; Wu, S. Generic functional modelling of multi-pulse auto-transformer rectifier units for more-electric aircraft applications. *Chin. J. Aeronaut.* **2018**, *31*, 883–891. [CrossRef]
18. Chen, J.; Shen, J.; Chen, J.; Shen, P.; Song, Q.; Gong, C. Investigation on the selection and design of step-up/down 18-pulse ATRUs for more electric aircrafts. *IEEE Trans. Transp. Electrif.* **2019**, *5*, 795–811. [CrossRef]
19. Yang, T.; Bozhko, S.; Asher, G. Functional modeling of symmetrical multipulse autotransformer rectifier units for aerospace application. *IEEE Trans. Power Electron.* **2015**, *30*, 4704–4713. [CrossRef]
20. Zhao, Y.; Huang, W.; Bu, F. DC voltage balancing strategy of a bipolar-output active rectifier for more electric aircraft based on zero vector redistribution. *IEEE Access* **2021**, *9*, 139657–139667. [CrossRef]
21. Li, Y.; Junyent-Ferre, A.; Rodriguez-Bernuz, J.M. A three-phase active rectifier topology for bipolar dc distribution. *IEEE Trans. Power Electron.* **2018**, *33*, 1063–1074. [CrossRef]

22. Rivera, S.; Lizana, R.; Kouro, S.; Dragicevic, T.; Wu, B. Bipolar dc power conversion: State-of-the-art and emerging technologies. *IEEE J. Emerg. Sel. Top. Power Electron.* **2021**, *9*, 1192–1204. [CrossRef]
23. Yan, S.; Yang, Y.; Hui, S.Y.; Blaabjerg, F. A review on direct power control of pulsewidth modulation converters. *IEEE Trans. Power Electron.* **2021**, *36*, 11984–12007. [CrossRef]
24. Zhang, Y.; Jiao, J.; Liu, J.; Gao, J. Direct power control of PWM rectifier with feedforward compensation of DC-bus voltage ripple under unbalanced grid conditions. *IEEE Trans. Ind. Appl.* **2019**, *55*, 2890–2901. [CrossRef]
25. Noguchi, T.; Tomiki, H.; Kondo, S.; Takahashi, I. Direct power control of PWM converter without power-source voltage sensors. *IEEE Trans. Ind. Appl.* **1998**, *34*, 473–479. [CrossRef]
26. Zhang, Y.; Gao, J.; Qu, C. Relationship between two direct power control methods for PWM rectifiers under unbalanced network. *IEEE Trans. Power Electron.* **2017**, *32*, 4084–4094. [CrossRef]
27. Sato, A.; Noguchi, T. Voltage-source PWM rectifier–inverter based on direct power control and its operation characteristics. *IEEE Trans. Power Electron.* **2011**, *26*, 1559–1567. [CrossRef]
28. Yan, S.; Chen, J.; Yang, T.; Hui, S.Y. Improving the performance of direct power control using duty cycle optimization. *IEEE Trans. Power Electron.* **2019**, *34*, 9213–9223. [CrossRef]
29. Zhang, Y.; Qu, C.; Gao, J. Performance improvement of direct power control of PWM rectifier under unbalanced network. *IEEE Trans. Power Electron.* **2017**, *32*, 2319–2328. [CrossRef]
30. Zhang, Y.; Qu, C. Table-based direct power control for three-phase AC/DC converters under unbalanced grid voltages. *IEEE Trans. Power Electron.* **2015**, *30*, 7090–7099. [CrossRef]
31. Hamed, H.A.; Abdou, A.F.; Acharya, S.; El Moursi, M.S.; EL-Kholy, E.E. A novel dynamic switching table based direct power control strategy for grid connected converters. *IEEE Trans. Energy Convers.* **2018**, *33*, 1086–1097. [CrossRef]
32. Huang, J.; Guo, F.; Wen, C.; Yang, B.; Xiao, J. A direct power control strategy for AC/DC converter based on best switching state approach. *IEEE J. Emerg. Sel. Top. Power Electron.* **2018**, *6*, 2273–2286. [CrossRef]
33. Eloy-Garcia, J.; Alves, R. DSP-based direct power control of a VSC with voltage angle estimation. In Proceedings of the 2006 IEEE/PES Transmission & Distribution Conference and Exposition: Latin America, Caracas, Venezuela, 15–18 August 2006.
34. Chen, B.S.; Joos, G. Direct power control of active filters with averaged switching frequency regulation. *IEEE Trans. Power Electron.* **2008**, *23*, 2729–2737. [CrossRef]

Disclaimer/Publisher's Note: The statements, opinions and data contained in all publications are solely those of the individual author(s) and contributor(s) and not of MDPI and/or the editor(s). MDPI and/or the editor(s) disclaim responsibility for any injury to people or property resulting from any ideas, methods, instructions or products referred to in the content.